

# **R12.5 Solar Simulator Evaluation Report**

---

## **Project SFERA**

### **Deliverable 12.5**

**This document was prepared by**

**Ivo Alxneit (PSI) and Gerd Dibowski (DLR)**

**August 2011**

**Solar Facilities for the European Research Area**

# Abstract

Arc lamp based solar simulators have only recently been built at different research institutes. At present, only a limited knowledge base and little practical experience are available with regard to their handling, their performance, and their long time maintenance requirement. SFERA WP12.3 addresses these issues by performing the **experimental characterization of solar simulators** (task 3A) and by analyzing **solar simulator specific components/issues** (task 3B) for the solar simulators installed at PSI and at DLR.

The spectrum of the concentrated radiation has been recorded at the two high flux solar simulators (HFSS). At PSI, the spectra have been recorded in the range 350-1600 nm at different location inside the spot [1,2]. We found that the spectrum consists approximately of a suitably scaled black body spectrum of about 6000 K with the Xe emission lines superimposed. While at the center of the spot significantly more UV radiation is present compared with the outer regions of the spot the relative contribution of Xe emission lines is lower at the center of the spot. At DLR, the average spectrum of the concentrated radiation was recorded in the range 400-1000 nm and a very similar spectrum as at PSI's HFSS was obtained. DLR's high resolution data was complimented by data obtained during the filter-radiometer campaign. In this campaign the concentrated radiation was analyzed with a commercial radiometer in a few, narrow wavelength interval selected by narrow band transmission filters. In addition, a commercial UV radiometer was used to assess the amount of UV-A and UV-B radiation present. It was found that in the vicinity of the spot a high intensity of UV radiation significantly exceeds the limits imposed by [5,6]. Thus, personnel exposed to this radiation must take precautions to protect their eyes and exposed skin.

For both solar simulators conversion of the superposition of Gaussian spots into a more even, pill-box shaped flux distribution was addressed with optical mixers / flux guides: tubes with a square cross section and reflecting inner surfaces were evaluated by ray tracing models and build. Additionally, the flux distribution at DLR's HFSS was measured for the case when the individual foci of the ten reflectors were not anymore superimposed but evenly distributed on a  $140 \times 140 \text{ mm}^2$  target.

Issues with the stability of the reflective coating experienced initially at DLR's simulator could be solved by the manufacturer after extensive testing of different coatings. Some ageing of the lamps (decreased intensity) has been observed at DLR. No such deterioration of the lamp performance as been observed at PSI so far. Note however, that the lamps at PSI are presently operated at  $12.2 \text{ kW}_{el}$  instead of the rated  $15 \text{ kW}_{el}$ . We expect this to have a beneficial effect on the effective life time of the lamps.

A new pyrometric temperature measurement method has been developed at PSI [3] and demonstrated in a laboratory setup. An initial attempt to implement the method at PSI's HFSS failed due to electrical interferences by the high voltage transmission line running close to the solar simulator.

Overall it can be stated that the solar simulators already prove to be very valuable and reliable instruments for weather independent and reproducible testing of solar receivers for solar electricity production, for solar chemical reactors and for other applications.

# Table of Contents

<b>1</b>	<b>Introduction.....</b>	<b>4</b>
<b>2</b>	<b>Characterization of solar simulators.....</b>	<b>7</b>
2.1	Performance of the ellipsoidal reflectors.....	7
2.1.1	Modeling results with OptiCAD® (DLR).....	8
2.2	Experimental campaigns at the different solar simulator sites.....	10
2.2.1	Filter – Radiometer Campaign at DLR's HFSS.....	10
2.2.2	High resolution data (DLR and PSI).....	14
2.2.3	Results of initial UV-Measurements at DLR.....	18
<b>3</b>	<b>Solar simulator specific components/issues.....</b>	<b>20</b>
3.1	Design and test methods that are capable of generating a flat flux density distribution profile .....	20
3.1.1	OMX – PSI's optical mixer.....	20
3.1.2	DLR's flux guide – Determination of the flux guide geometry with OptiCAD®.....	23
3.1.3	Defocusing.....	26
3.2	Assessment of aging of simulator reflectors and arc lamps by performing periodic measurements.....	28
3.3	Pyrometric temperature measurement in solar simulators (PSI).....	31
3.4	Avoidance of electromagnetic disturbances due to rectifiers and arc lamps.....	34
<b>4</b>	<b>Conclusions and recommendations for future high flux solar simulators.....</b>	<b>34</b>
	<b>References.....</b>	<b>36</b>

# 1 Introduction

Xenon arc lamps, favored by commercial solar simulator manufacturers, can be filtered to have an emission spectrum closely matching the one of terrestrial sunlight. They are available in high power single bulb configurations which can be coupled with a single ellipsoidal mirror, resulting in a tightly controlled spot size [4]. However, high power Xenon arc-lamps and their associated drive electronics are expensive products, with nearly 10 times the costs-per-watt than commodity light sources.

The 150 kW<sub>el</sub> solar simulator installed at PSI is the first installation world-wide that applies several short arc lamps, each with its individual reflector where the concentrated radiation of all lamp/reflector units is superimposed at a common focal point [4]. At this focal point a peak flux of about 1.1 kWcm<sup>-2</sup> has been measured. In Figures 1 and 2 the geometry of the simulator is reported with only the major components shown. The venetian blind type shutter, initially not installed, is not shown.

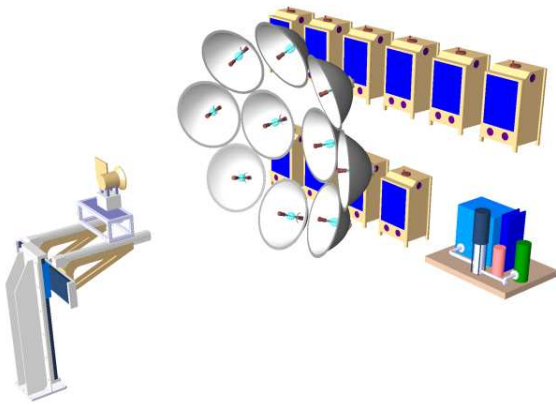


Figure 1:

*Schematic of PSI's solar simulator. Only lamp/reflector units, power supplies, cooling system and reactor on x-y-z translation stage shown.*

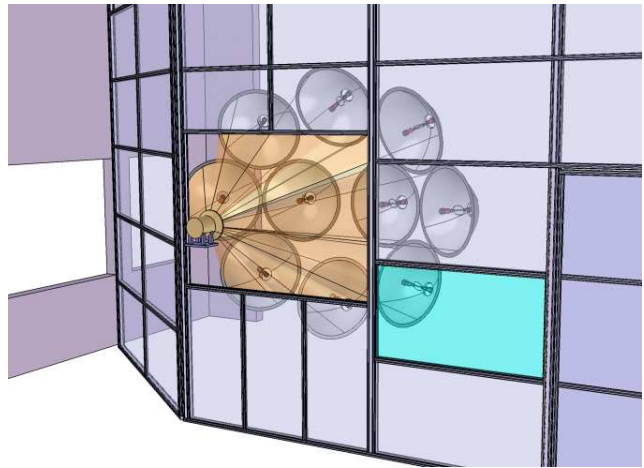
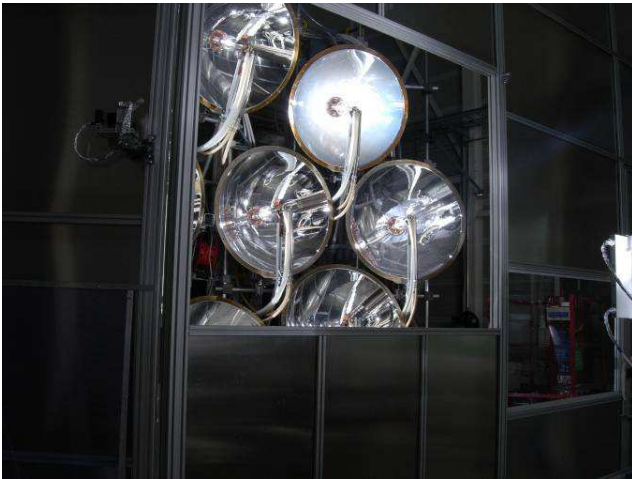


Figure 2:

*Schematic of PSI's solar simulator that includes protective housing of lamp array and window to control room.*

Figure 3 shows the array of individual lamp/reflector units with a single lamp in operation as seen from a position close to the spot. Clearly visible are cooling water and electrical feeds leading to the front electrodes. Again, the shutter, seen in the fully closed position in Figure 4, was not yet installed when this picture was taken. This shutter is used to control the radiative power available from the simulator fast and with a high resolution. A cruder control of this important process variable is performed by selection the number of arc lamps used. The shutter is build from aluminum blades that are rotated. Their rotation axes are on a circular arc fragment because the shutter has to be placed at a position where the radiation is converging. This is in contrast to e.g. the shutter installed at PSI solar furnace. Here, the shutter can be placed between heliostat and parabolic dish i.e. in a parallel beam.



*Figure 3:*

*View of lamp/reflector array with one lamp in operation(PSI).*



*Figure 4:*

*View of shutter (fully closed) installed between lamp/reflector array and protective window(PSI).*

Applied at the DLR HFSS [5] are ten  $6 \text{ kW}_e$  Xenon short-arc lamps supplied by Osram (OSRAM 6000 W/HSLA OFR). In contrast to the  $15 \text{ kW}_e$  water-cooled Xenon short-arc lamps (Ushio UXW 15000 W) installed at PSI's HFSS, these lamps can be cooled by air. This reduces the complexity of such a system considerably.



*Figure 5:*

*DLR's solar simulator with all lamps in operation*

In Figure 5 DLR's solar simulator can be seen in operation. A complete unit with one lamp and all mechanical devices and electrical support as installed at DLR, from here onwards referred to as „Xenon-block“ is reported in Figure 6.

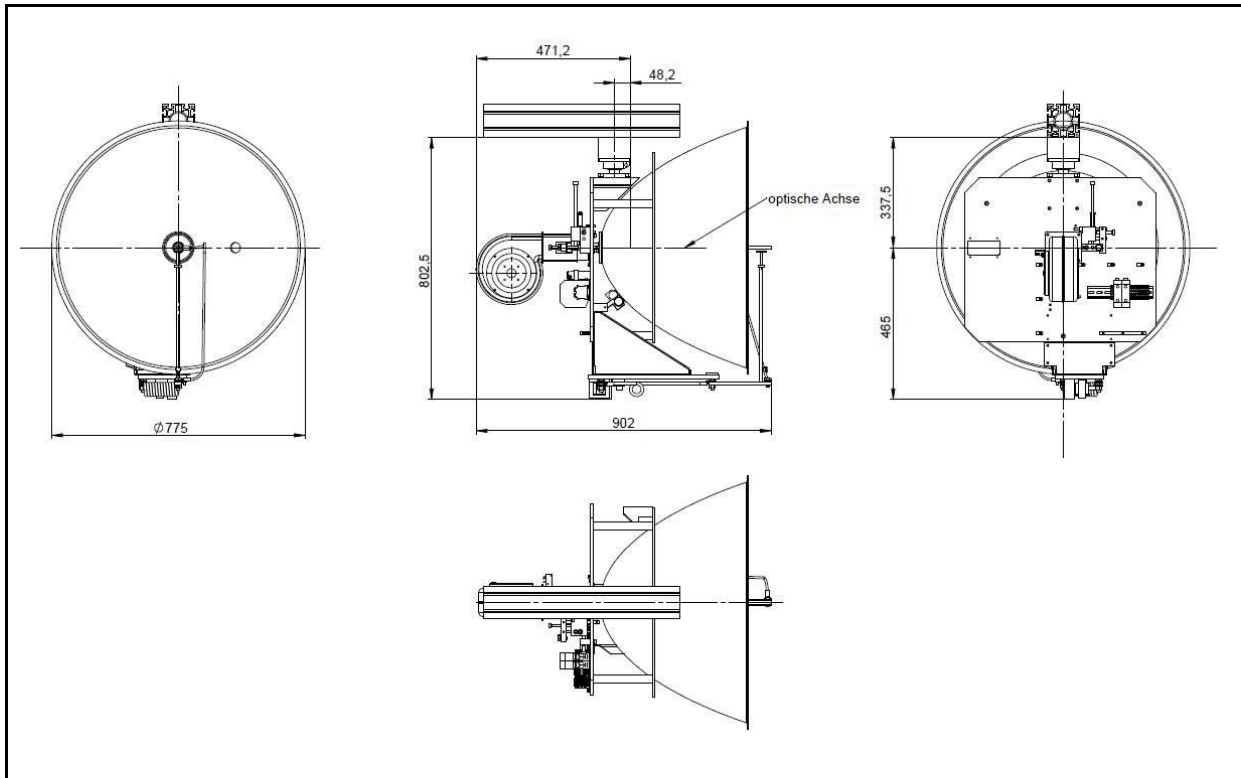


Figure 6:

*DLR HFSS Xenon-block.*

## 2 Characterization of solar simulators

Primary objectives are:

- spectral characterization of the concentrated radiation at the spot (average spectrum) and, optionally, spatially resolved spectra.
- assessment of the UV contribution near the spot (safety considerations).

Existing equipment (various detectors, spectrograph, radiometers) is used for these purposes.

### 2.1 Performance of the ellipsoidal reflectors

Before starting the assembly of the high-flux solar simulator (HFSS) at DLR it was deemed necessary to perform tests concerning the accuracy of the curvature of the ellipsoidal mirrors and the quality of the reflective coating available. Reflectors at DLR and PSI were produced by the same manufacturers (basic reflector: Heggli & Gubler; coating: Kaltbrunner, both from Switzerland). Due to lack of available experience and of published data it was decided to simulate the mirror with ray-tracing methods (OptiCAD<sup>®</sup>) and to compare the results with measurements of the experimentally determined flux density.

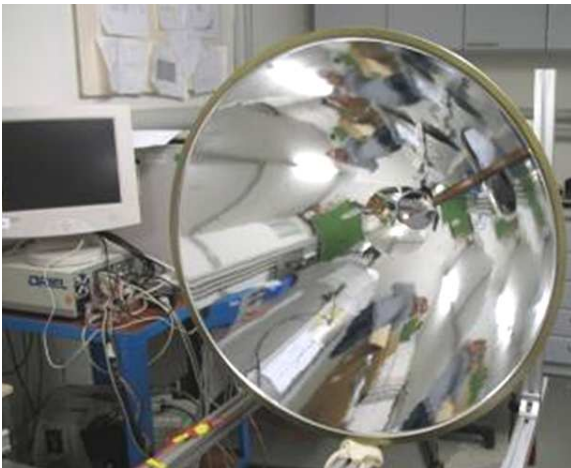


*Figure 7:*

*Evaluation of one reflector at DLR.*



*Figure 8:*

*Reflection on a plasma coated Al<sub>2</sub>O<sub>3</sub> target at DLR.*

Results always refer to the combination of lamp and reflector as one unit and thus depend on the (possibly) changing characteristics of lamps and the reflective coatings with age, on the quality of the reflective coating, and on the general surface properties of the reflectors. Further interest covers the influence of aging of lamps and reflectors on the spectrum and the dynamics of the spectrum during start up until steady state operation is achieved. Preliminary measurements seem to indicate that the lamps (OSRAM 6000 W/HSLA OFR at DLR) need significantly longer to achieve steady state operation than claimed by the manufacturer. This information might become important for experiments requiring short exposure times. For safety reasons it will be important to assess how much UV radiation is emitted by these lamps. Preliminary results of UV-A and UV-B measurements in the area in the vicinity of the spot at DLR show the presence of up to twenty times more UV radiation than claimed by the manufacturers.

### 2.1.1 Modeling results with OptiCAD® (DLR)

OptiCad is used to model the performance of a Xenon-block by analyzing the flux distribution on a flat target places at the location of the spot. OptiCAD®'s rendering process involves randomly generated rays propagated through the optical system. Processes such as e.g. reflection, absorption, or refraction are included in the treatment. It is thus possible to compare the simulation results with measured data to estimate the flux distribution achieved by the complete assembly.

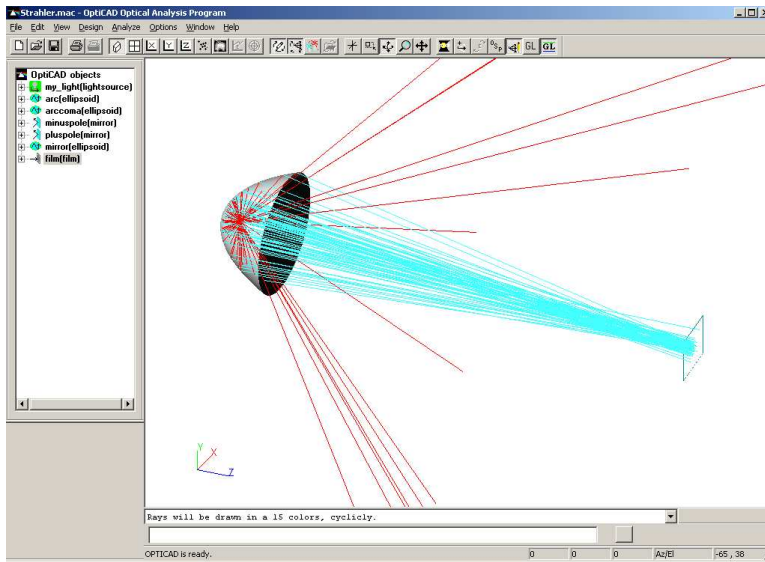


Figure 9:

Typical result of calculation the concentration on target. Red vectors symbolizes non-reflected rays.

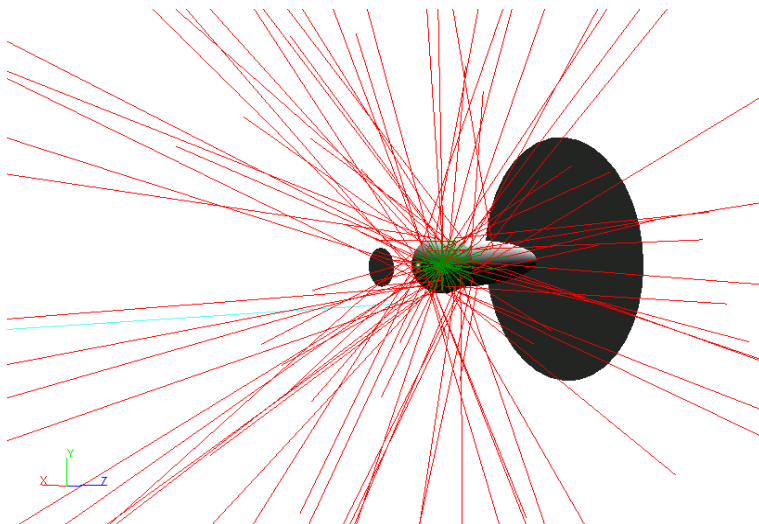


Figure 10:

Modeled plasma core and boundary conditions in the primary focus of the reflector (blocking due to electrodes).

Figure 9 exemplifies the result of a calculation by OptiCAD®. Note, that it is very important to correctly model the geometry of the light source (plasma arc) as well as the geometric restrictions imposed by the tips of the electrodes as seen in Figure 10.

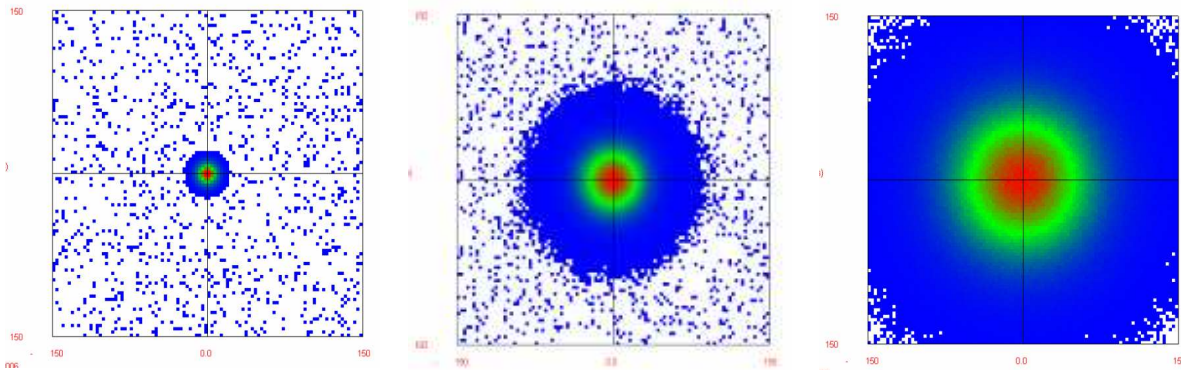


Figure 11:

Ray tracing results (flux distribution on target at spot) with different assumed reflection errors  $\sigma$ .

$\sigma = 0 \text{ mrad}$

$\sigma = 5 \text{ mrad}$

$\sigma = 12 \text{ mrad}$

Figure 11 reports calculated flux distributions for different values of  $\sigma$  (Gauss error) of the reflector. One notes, that the quality of the reflector surface is decisive for the optical quality of the system. The average roughness  $R_a$  should not exceed  $\frac{1}{4}$  of the used wavelength to avoid diffuse stray light. Below this value regular directed reflection at the mirror surface dominates. A maximum surface error of up to 5 mrad is acceptable and leads to a spread of the spot on the target of near 15 mm at a focal length of 3 m.

To compare the ray tracing results with the measured distribution a spot light was positioned in primary focus of the reflector (F1) and the flux distribution on the target at F2 was recorded (see Figure 12).

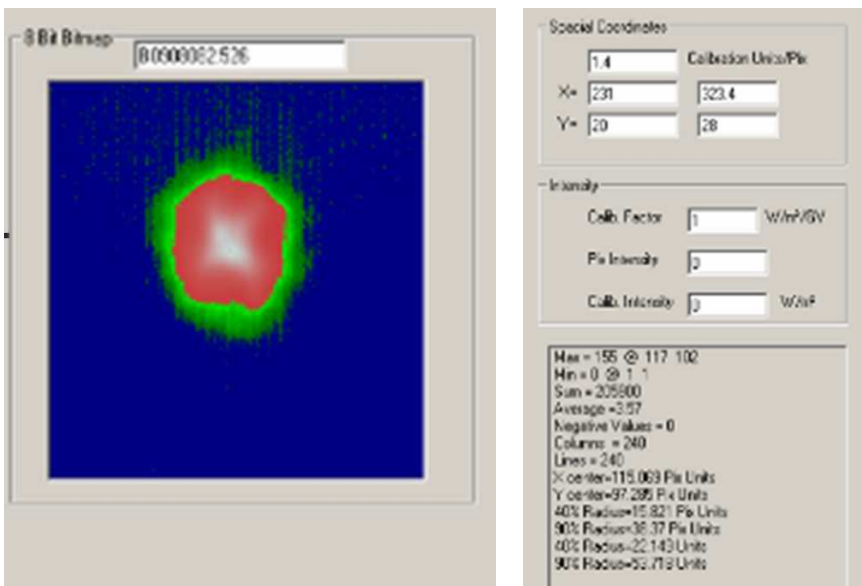


Figure 12:

Measured flux distribution on target to be compared with the OptiCAD® results.

Figure 13 reports a comparison of horizontal cross sections for modeled and measured (see Figure 12) flux distributions. A reflection error of  $\sigma = 5 \text{ mrad}$  applied in the model accurately describes the measured data.

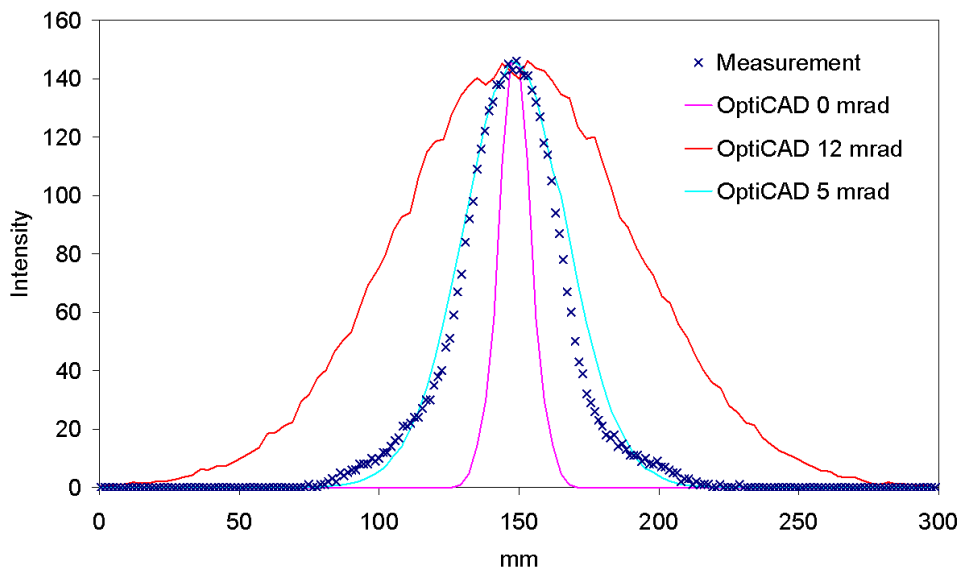


Figure 13:  
Horizontal cross sections through measured and modeled flux distributions.

A similar evaluation of PSI's HFSS has been published in [4].

## 2.2 Experimental campaigns at the different solar simulator sites

### 2.2.1 Filter – Radiometer Campaign at DLR's HFSS

The global average spectrum of DLR's HFSS was measured with an absolute value radiometer (National Light Inc., IL1700. See Figure 16) equipped with a SED 033 silicon detector (Figure 19). Narrow band pass filters (Andover, approximately 10 nm FWHH. See Figure 17) were put in front of the detector to select a narrow wavelength interval. A schematic representation of the geometry for these measurements is reported in Figure 14. To convert the radiometer readings to average flux values on the water-cooled reference target the solid angle  $\Omega_{\text{eff}}$  has to be known (see Equation 1) and it has to be verified that the target is indeed Lambertian (see Figure 15).

The solid angle  $\Omega_{\text{eff}}$  (steradians) can be calculated with Eqn. 1. The Distance from the front surface of the detector SED 033 to the detector surface amounts to 6,5 mm, the radius of the SED 033 is  $R = 7,5$  mm.

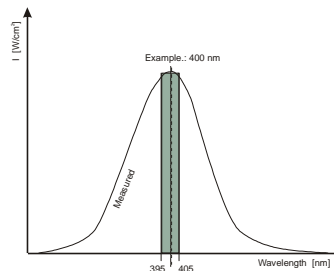
$$\Omega_{\text{eff}} = \frac{\pi \cdot r^2}{z^2 \cdot \left(1 - \frac{(R^2 + r^2)}{z^2}\right)} \quad [\text{Eqn. 1}]$$

The radius of the Lambertian source (spot) is  $r$ . The distance  $z = L1 + L2 + 6,5$  mm with:

L1: distance spot – aperture

L2: distance aperture – detector front

The total irradiation can be calculated by integrating the measured peaks ( $\pm 10$  nm) of each filter transmission result



$$A_{\text{strip}} = \int_{\lambda-5\text{nm}}^{\lambda+5\text{nm}} T(\lambda(\lambda))$$

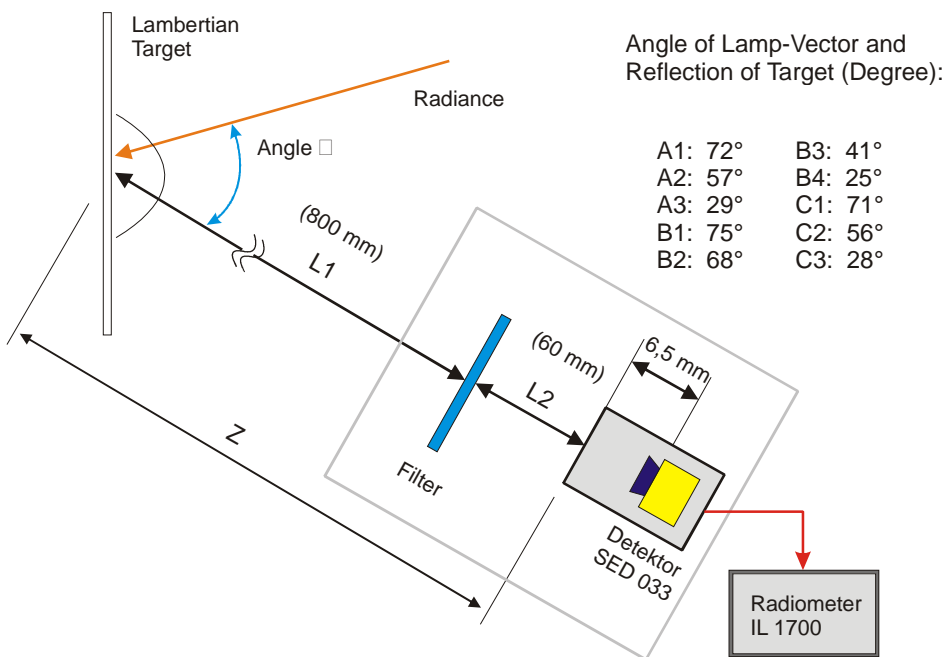


Figure 14:  
Measurement geometry for filter-radiometer campaign at DLR's HFSS.

Observation angle for lamps A1-C3 is indicated in table.

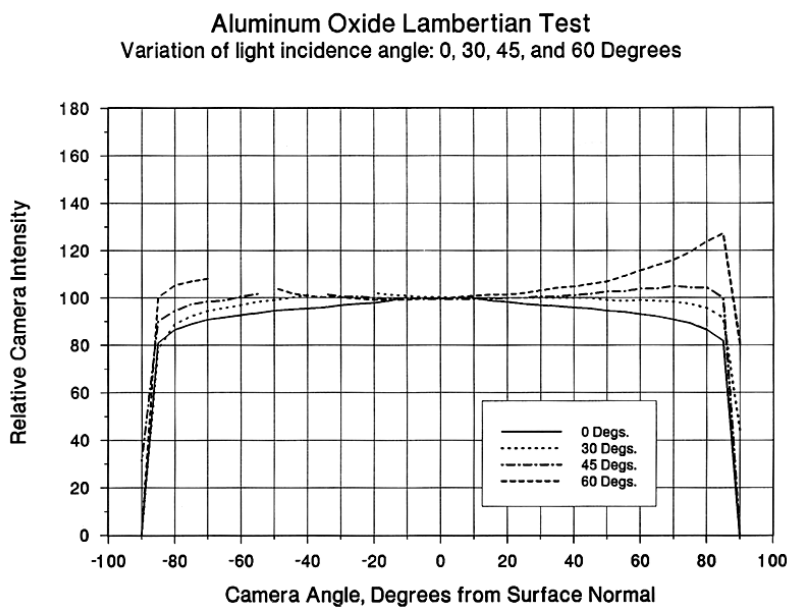


Figure 15:  
Verification of assumption of a diffuse target (Lambertian).

The research radiometer IL 1700 is designed specifically to measure photo detector currents. It maintains linearity over a 10 decade dynamic range. The IL 1700 achieves this dynamic range through the use of a proprietary front end amplification system. The floating, current to current amplifier boosts the photo-conductor current directly, without the constant gain changes that compromise linearity in transimpedance amplification schemes. Because of its unique current measurement circuitry, the IL 1700 is the only radiometer in the world that can performance autoranging during exposure integrations, over its entire 10 decade dynamic range.



Figure 16:  
Radiometer IL 1700.



Figure 17:  
Narrow band pass filter with a typical transmissions-half-bandwidth of 10 nm.

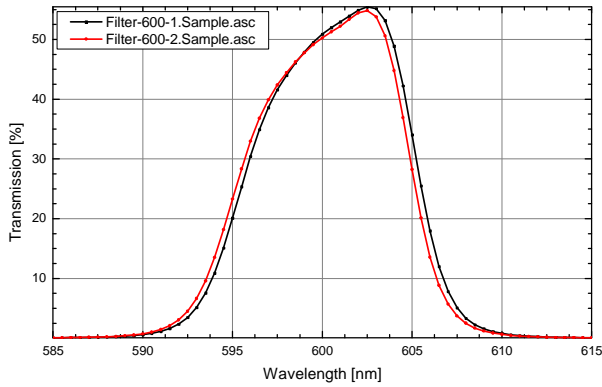


Figure 18:  
Test configuration during the campaign.



Figure 19:  
Filter box (open and closed) containing detector SED 033 (rear) and narrow bandwidth transmission filter (front).

The transmission curves for all filters used in this campaign were determined beforehand on a UV/VIS spectrometer (PerkinElmer Lambda 900, UV WinLab 5.2.0.0646). Each filter was measured twice with the measurement spot placed a different part of its usable area. In Figure 20 (left) the two transmission curves for the filter centered at 600 nm is reported. A comparison of all transmission curves is reported in Figure 21 and key results are tabulated in Figure 20 (right).



nominal [ nm ]	Wavelength [ nm ]	Transmission [ % ]
1014	1011	14,46073
1000	1000,5	25,05921
980	979,5	23,64618
960	959,5	31,67973
940	940	19,70942
920	920	32,19451
900	900,5	31,13734
880	880	28,31011
860	860	43,56831
840	841	68,82498
820	822	53,60486
800	803,5	66,05536
780	783	59,66798
760	759,5	56,23428
740	738	61,43851
720	720	71,48885
700	702,5	57,92557
600	602,5	55,1684
500	498,5	59,72791
400	402,5	53,45368

Figure 20:

(top) Example of filter transmission curve. (left) Table of measured filter specifications ( $\lambda_{peak}$  and  $T_{peak}$ ).

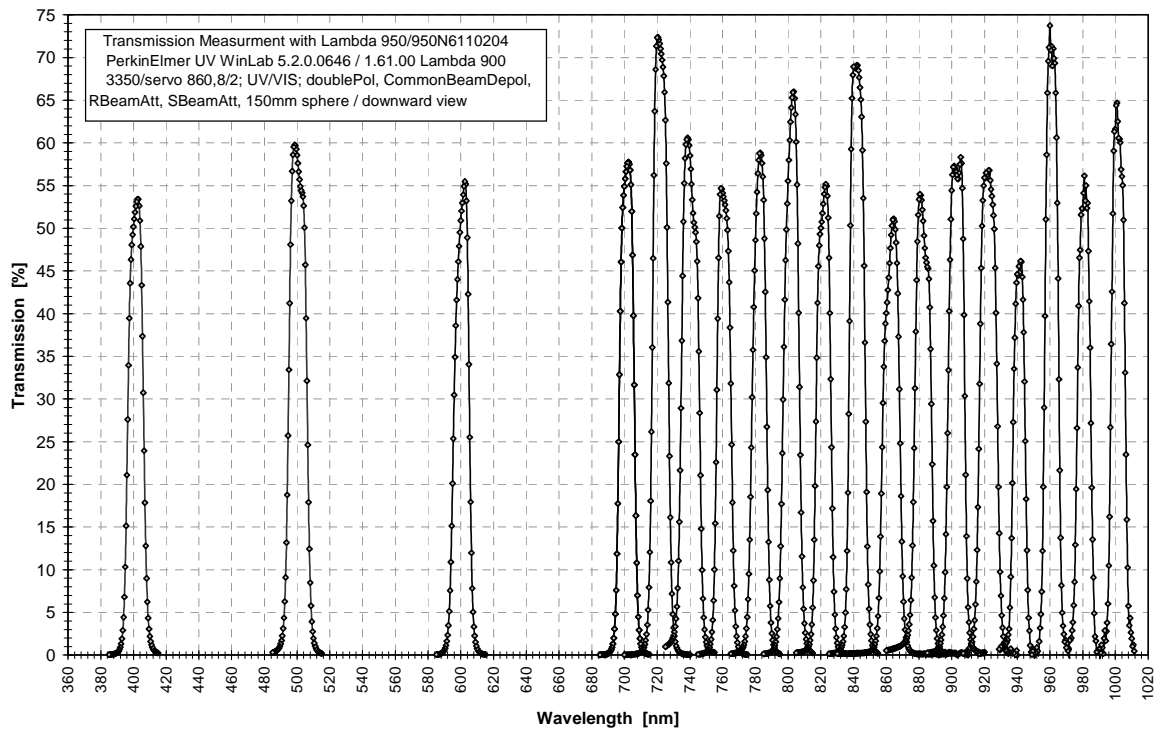


Figure 21:

Transmission curves of all filters used in campaign.

The average spectrum of the concentrated radiation of DLR's HFSS was recorded between 400 and 1014 nm applying the set of 20 band pass filters characterized in Figures 20 and 21. A compilation of all data is reported in Figure 22. The labels in its legend refer to the slightly different measurement geometries according to Figure 14.

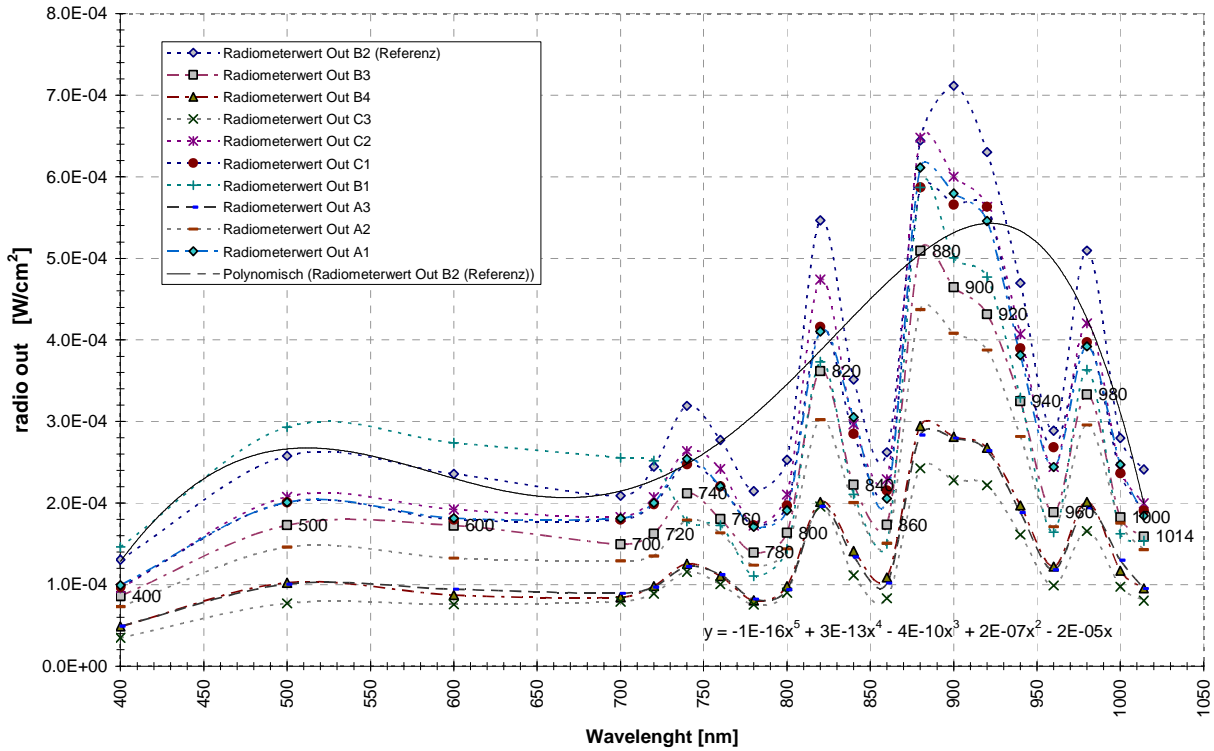


Figure 22:

Compilation of results of filter-radiometer campaign to measure the average spectrum of the concentrated radiation of DLR's HFSS with all 10 lamps operated. Spline interpolation of data is also indicated.

A comparison to PSI's high resolution data is reported in Figure 28.

### 2.2.2 High resolution data (DLR and PSI)

The spot of PSI's solar simulator with a single lamp in operation and with all ten lamps in operation was characterized spectrally and spatially resolved. Details can be found in [1, 2]. In the following the main results are briefly summarized.

Radiation reflected by a water-cooled Al<sub>2</sub>O<sub>3</sub>-coated target was sampled from a spot of 3.5×6 mm<sup>2</sup> (compared with a FWHM of the region of concentrated radiation of about 5 cm). Spectra collected in the range 350-1000 nm were recorded with a diode array at a resolution of approximately 0.5 nm. Spectra between 800 nm and 1600 nm were recorded by a Ge detector at a resolution of 2 nm (below 1000 nm) and 10 nm (above 1000 nm). The wavelength dependent sensitivity of the setup was corrected relative to a spectral irradiance standard (Oriel 63358).

Spectra collected at different radial distances from the center of the spot (*r*), divided by the spectrum

corresponding to  $r = 0$  and the normalized at an arbitrary chosen wavelength of 700 nm (between Xe emission lines) are reported in Figures 23 and 24 for a single lamp and for all lamps operating, respectively. It is evident from these figures that the spectrum of the concentrated radiation varies as function of  $r$ . The relative intensity of the UV contribution to the spectrum decreases with increasing  $r$ . In contrast, the relative intensity of the Xe emission lines increases with increasing  $r$ .

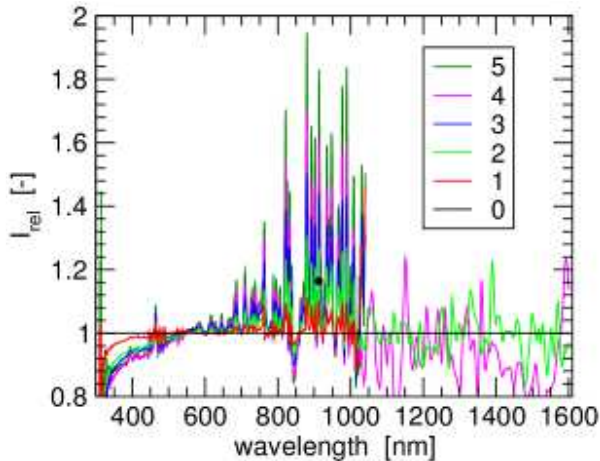


Figure 23: Spectral characterization as function of radial distance from center (0-5cm) with one lamp in operation

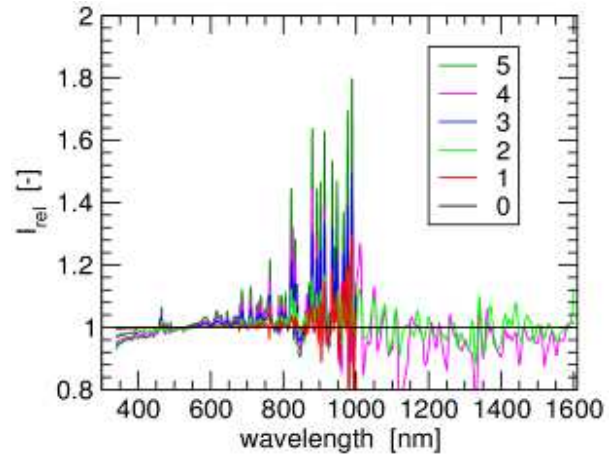


Figure 24: Spectral characterization as function of radial distance from center (0-5cm) with all lamps in operation

All spectra can be decomposed into a broad background upon which the emission lines of Xe are superimposed as illustrated in Figure 25. Interestingly, this decomposition works well for both situations studied, a single lamp in operation and all ten lamps operating. In all cases the continuous background can be well approximated by a properly scaled black body spectrum that corresponds to a temperature of  $6000 \pm 200$  K. Note, that the discrepancy between the measured spectrum and the black body curve below 400 nm is mostly due to absorption by the protective window mounted between the lamps and the target as well as by the fused silica envelope of the lamp.

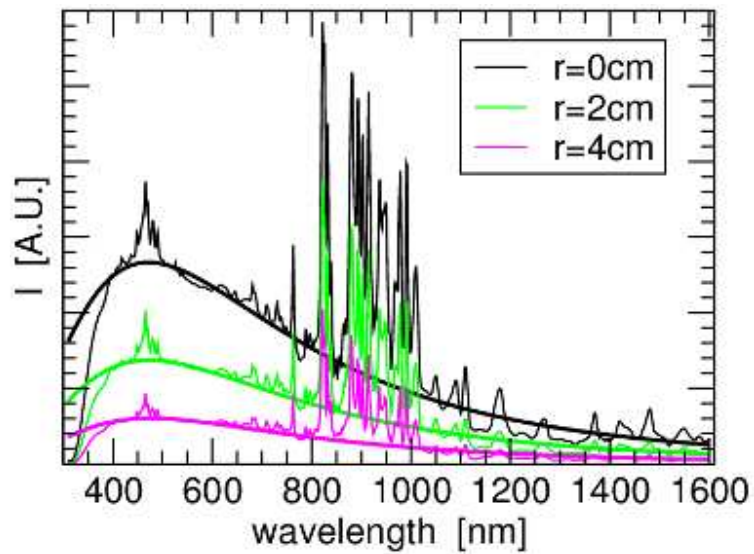


Figure 25: Phenomenological decomposition of spectra into black body spectrum ( $T=6000\pm 200$  K) and Xe emission lines.

At the DLR HFSS, spectral measurements were carried out using a Merlin lock-in amplifier in combination with a MS 257 monochromator (Oriel Corp.) as depicted in Figure 26.

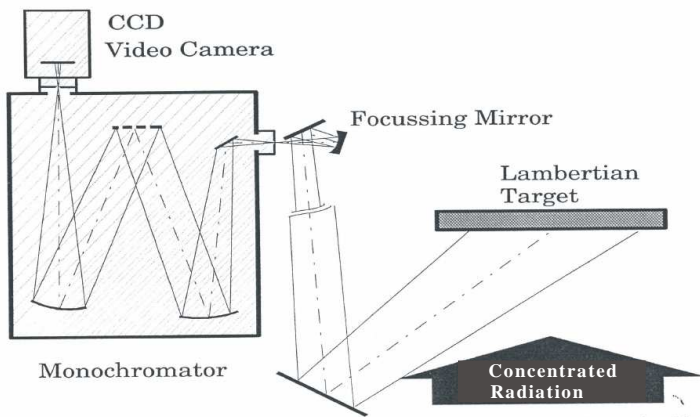


Figure 26:

Measurement setup. The image of the spot on the Lambertian target is transferred onto the monochromator entrance slit which selects the location of the beam cross section (resolution about  $\pm 1$  mm) to be analyzed.

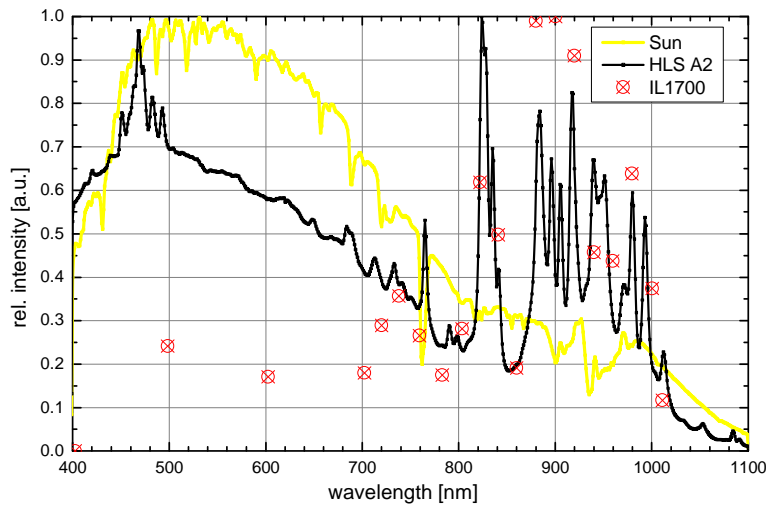


Figure 27:

Example of results of the measurement campaign at DLR. Continuous spectrum (black) compared to radiometer data red and terrestrial solar spectrum (yellow). Spectra are normalized with respect to their peak values.

The continuous spectra ( $\Delta\lambda \approx 1 \text{ nm}$ ) of the DLR HFSS are similar to the terrestrial solar spectrum but exhibit much higher intensities in regions where Xe emission lines dominate (see Figure 27). A comparison to the radiometer data reported below is much more difficult. As the filters exhibit a rather wide transmission (about 10 nm) compared to the emission lines some of the data points might represent the sum of several individual lines thus distorting the intensity information.

The average spectra corresponding to the concentrated radiation at the spot in the DLR solar simulator was also recorded with a radiometer (radiometer data). Narrow bandwidth transmission filters (typically 10 nm FWHM) were mounted in front of the detector to select a narrow wavelength band. In Figure 28 a comparison of the spectra of the concentrated radiation in the two high flux solar simulators is reported. For an easier comparison the spectra are normalized with regard to their peak values. The spectra agree rather well with each other above about 600 nm where the contribution of the Xe emission lines dominates. Below 600 nm PSI's simulator exhibits intensities higher by about a factor of 2 but some spectral differences between the two simulators are to be expected as they are operated with different types of arc lamps.

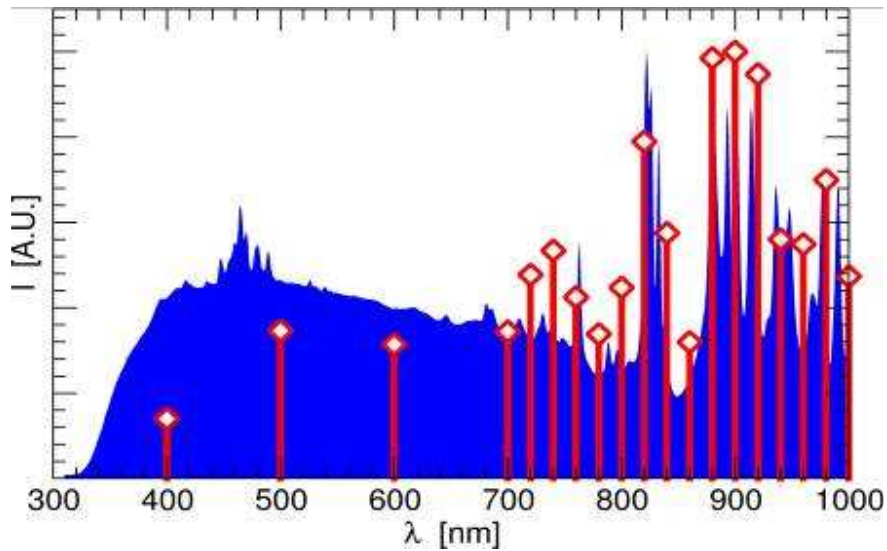


Figure 28: Normalized spectra of PSI's (blue, continuous data) and of DLR's (red, discrete wavelengths) solar simulators.

### 2.2.3 Results of initial UV-Measurements at DLR

Working with concentrated solar or artificial solar radiation employees may be exposed to higher levels of ultraviolet (UV) radiation. The measured UV exposure values are compared with the exposure limits for artificial optical radiation as stated in BG Information BGI 5006. These limits will remain in force in the future following transposition of the EU Directive 2006/25/EC "Artificial Optical Radiation" and the international Commission on Non-ionizing Radiation protection ICNIRP [6, 7].

For preventing from acute or long term damages the spectral weighting-factor  $S(\lambda)$  is determined which evaluate the UV irradiation in a range of 180 to 400 nm (UV-A/B/C) during a daily working exposure-time of 8 hours. In between this time a radiation of  $H_{\text{eff}} 30 \text{ J/m}^2$  may not be exceeded. The spectral weighting-factor  $S(\lambda)$  describes the effect on human eyes and skin depending on the wavelength. At a uniform exposure over a time period of 8 hours the limit is reached at an effective irradiance of  $E_{\text{eff}} = 1 \text{ mW/m}^2$ .

Measurements of UV-A and UV-B were carried out with an UV-VIS Radiometer RM-21 (Dr. Gröbel) with an accuracy for both sensors of  $\pm 7\%$  (see Figure 29). The data were obtained at the same position as the one taken with the radiometer IL 1700.

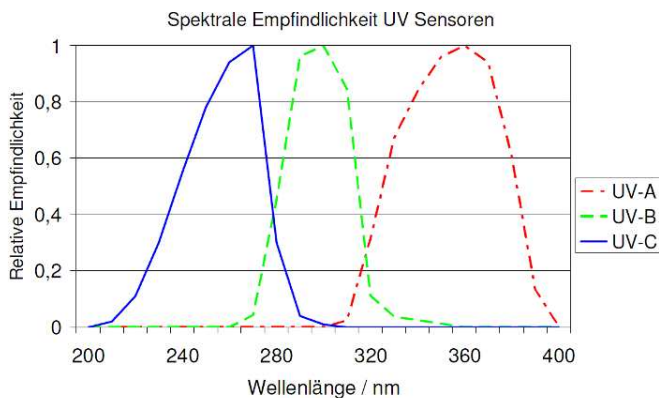


Figure 29:

Spectral sensitivity of the UV-A and UV-B measuring head

To evaluate the effect of the radiation onto the human body (eyes and skin) the measured data have to be corrected with the biological correction factors for UV-A (0.00183) and for UV-B (2.86). Raw data and corrected data are reported in Table 1.

Lamp	UVA [mW/cm <sup>2</sup> ]	UVB [mW/cm <sup>2</sup> ]	UVA [mW/cm <sup>2</sup> ] biologically active	UVB [mW/cm <sup>2</sup> ] biologically active
A1	1.4	0.74	2.56E-03	7.33E-03
A2	0.8	0.42	1.46E-03	4.19E-03
A3	0.48	0.26	8.78E-04	2.51E-03
B1	2.1	1.1	3.84E-03	1.10E-02
B2	1.1	0.54	2.01E-03	5.76E-03
B3	0.9	0.5	1.65E-03	4.71E-03
B4	0.37	0.2	6.77E-04	1.94E-03
C1	1.1	0.55	2.01E-03	5.76E-03
C2	0.81	0.44	1.48E-03	4.24E-03
C3	0.26	0.35	4.76E-04	1.36E-03

Table 1: Results of the UV-A and UV-B measurements. Raw data and data corrected with the biologically weighted factors.

The first results show that the limits according to ICNIRP are strongly exceeded (see Table 2). At DLR and at PSI so called ozone-free lamps are installed. These block radiation below about 200 nm. Still, these lamps emit strongly in the biologically active wavelength range. Based on our results, we conclude that the danger of UV radiation in the vicinity of the HFSS was underestimated in the past and that personnel exposed to this radiation must take precautions to protect their eyes and exposed skin. The measurement of UV will be continued.

Lamp	Threshold Value Exceeding Factor [ --- ]	
	UVA	UVB
A1	25.6	73.3
A2	14.6	41.9
A3	8.8	25.1
B1	38.4	109.9
B2	20.1	57.6
B3	16.5	47.1
B4	6.8	19.4
C1	20.1	57.6
C2	14.8	42.4
C3	4.8	13.6

Table 2: Threshold Value Exceeding Factor, the quotient of measured UV-radiance compared to the biological limit value by ICNIRP.

### 3 Solar simulator specific components/issues

#### 3.1 Design and test methods that are capable of generating a flat flux density distribution profile

Options include flux-guides or placement of the short arcs slightly out of focus.

Using multiple reflectors with their secondary focal points overlapping on a target, a Gaussian profile (see Figure 30) of the flux distribution is achieved. This flux distribution is often disadvantageous, because the energy is concentrated in a small spot on the sample. Thus, strong thermal gradients result in the material and ceramics e.g. can brake due to thermal stress. Often a flat distribution (pill box, see Figure 31) of the radiation is required to mimic the irradiation under normal natural conditions.

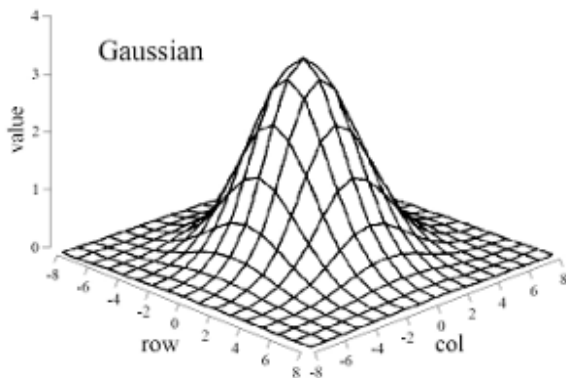


Figure 30:

Typical Gaussian distribution in the focal spot of a multi-mirror or multi reflector system.

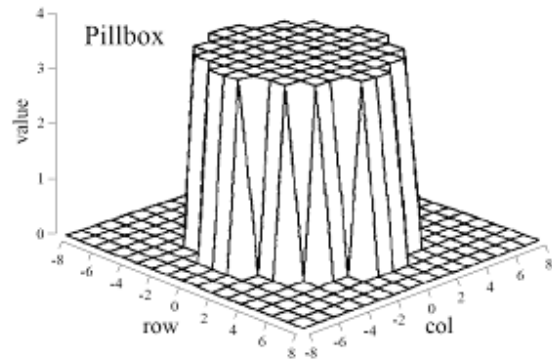


Figure 31:

Preferred flat flux-density distribution up to now achieved by placing sample out of focus or by "optical mixer" (flux guide).

##### 3.1.1 OMX – PSI's optical mixer

As an optical instrument to convert the near-Gaussian flux distribution of the spot of PSI's solar simulator a closed hollow channel with reflective inner walls was evaluated. The inlet of this mixing tube is placed in the focal plane of the solar simulator. Incident light undergoes multiple reflections before exiting thus improving the spatial and directional uniformity. Three mixing tube cross-sections were considered: circular, square and hexagonal. It was found that the square shape vastly outperformed the other cross-sections. This is explained by the fact that the degree of mixing is associated with the formation of skew rays within the tube. The closer the cross section resembles a circle, the fewer skew rays are generated since the incident beam diverges in a near circular manner. This analysis is therefore limited to mixing tubes with square cross-sections. A mixing tube of 150 cm in length with a  $15 \times 15 \text{ cm}^2$  cross-section was evaluated by ray tracing.

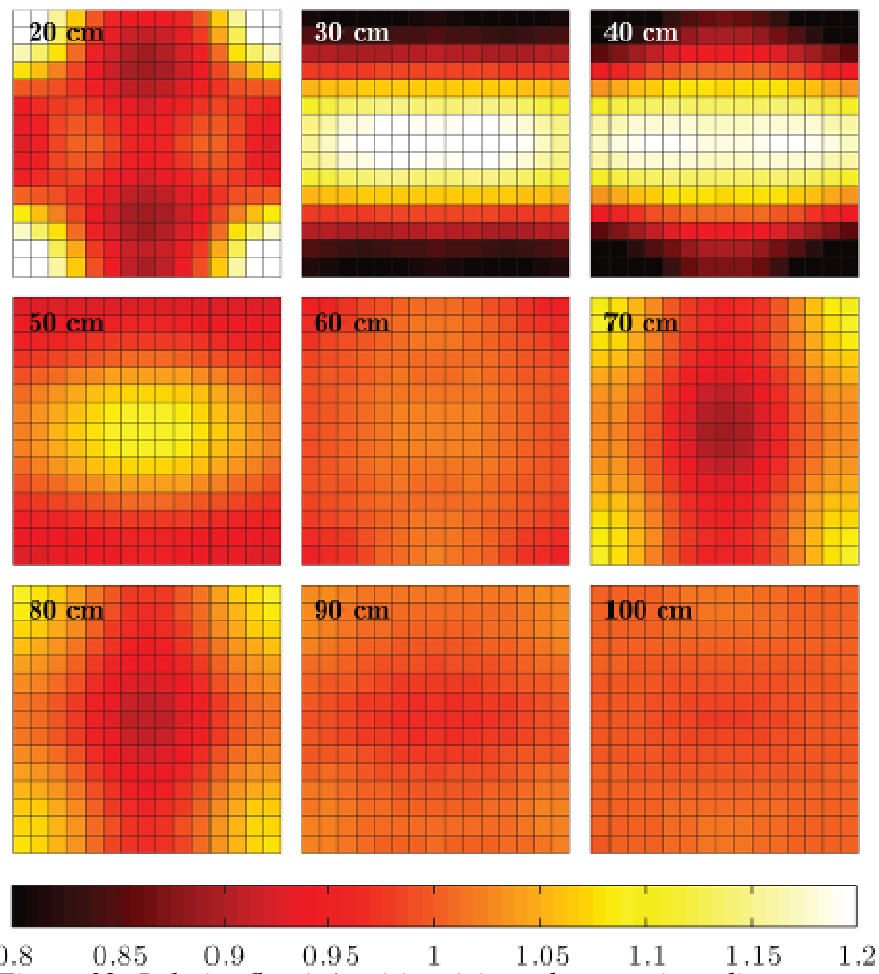


Figure 32: Relative flux ( $q/q_{avg}$ ) in mixing tube at various distances from entrance

In Figure 32 the flux distributions in the tube at various distances from its entrance are reported. It is seen that a local optimum for the homogeneity of the flux distribution exists for a tube length of 60 cm. To obtain a better uniformity, the tube length would have to be considerably increased to over 90 cm which would result in considerably higher absorption losses. Furthermore, a length of greater than 60 cm complicates the experimental setup due to the size restrictions at the HFSS. A tube length of 60 cm was therefore chosen as the final design reported in Figure 33.

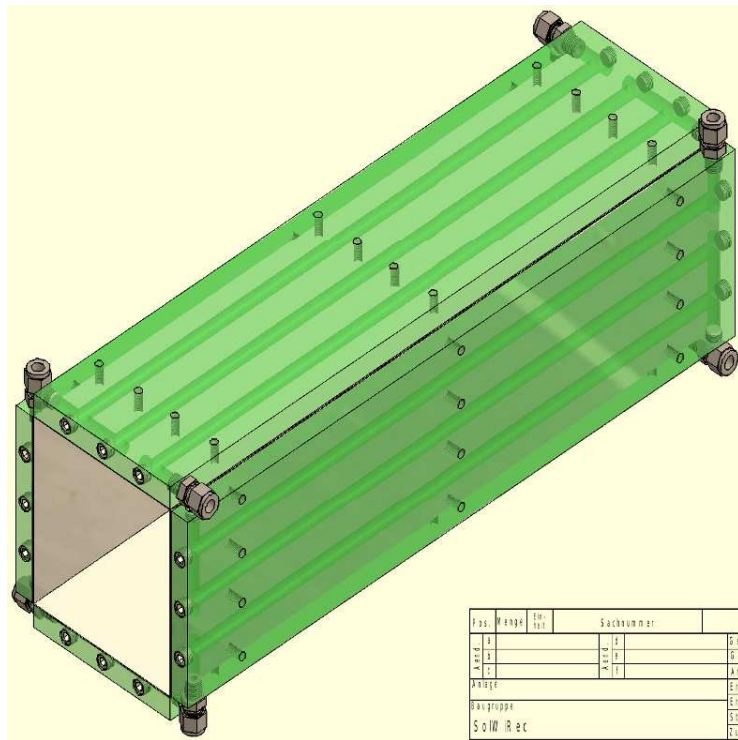


Figure 33: Final design of mixing tube made from water-cooled aluminum plates and reflective ( $r=0.95$ ) polymer film.

The preliminary experimental characterization of the mixing tube revealed that the flux at the exit of the 60 cm mixing tube varies by less than 10% and essentially confirmed the ray tracing data. Meanwhile another mixing tube ( $8 \times 8 \text{ cm}^2$ , see Figures 34 and 35) has been built and is e.g. used to test CPC-mirror systems within Work Package 13 of SFERA.



Figure 34: Front of  $8 \times 8 \text{ cm}^2$  mixer.



Figure 35: Exit of  $8 \times 8 \text{ cm}^2$  mixer.

### 3.1.2 DLR's flux guide – Determination of the flux guide geometry with OptiCAD®

By means of defined arrangements made out of flat metal mirror plates ("flux guide", see schematic in Figure 36) the flux distribution can be influenced. With an optimized arrangement of the flux guide a flux distribution close to a pillbox can be achieved. With the help of a ray tracing tools like OptiCAD® it is possible to study different configurations of the flux guide and to determine the optimum arrangement. In comparison to defocusing strategy (see below) the loss of power on the target is minimal using a flux guides because of the high reflectivity of the mirrors. The optimized design consists of right-angled or trapezoid-shaped actively cooled metal plates with polished inner sides or mirror surfaces. Rays entering the guide are reflected several times before they form a pill-box like flux distribution at its exit.

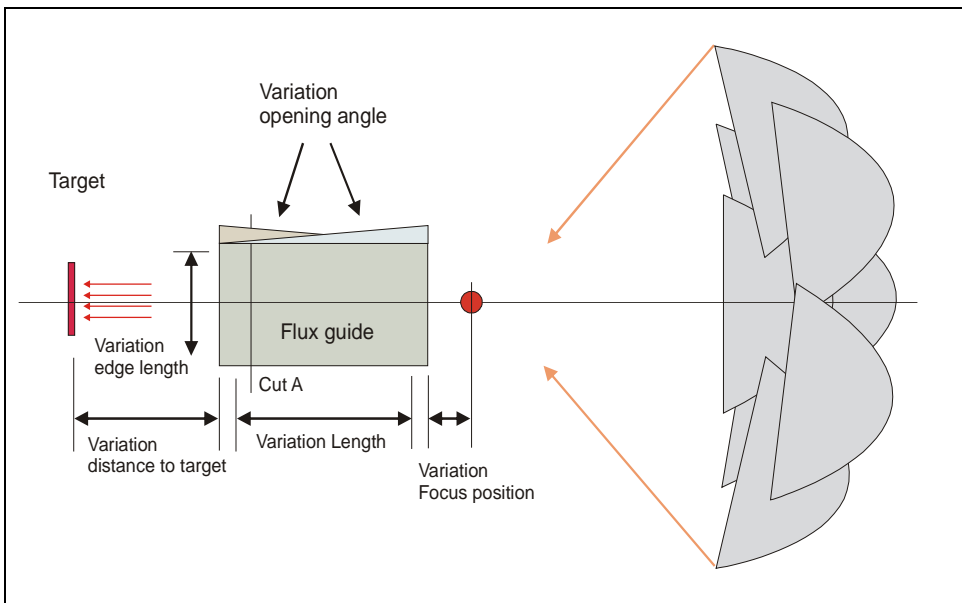


Figure 36:  
Diagram explaining the principle of the test device and the variation parameters.

The output of a simulation with OptiCAD<sup>®</sup> for a particular arrangement of the flux guide is reported in Figure 37.

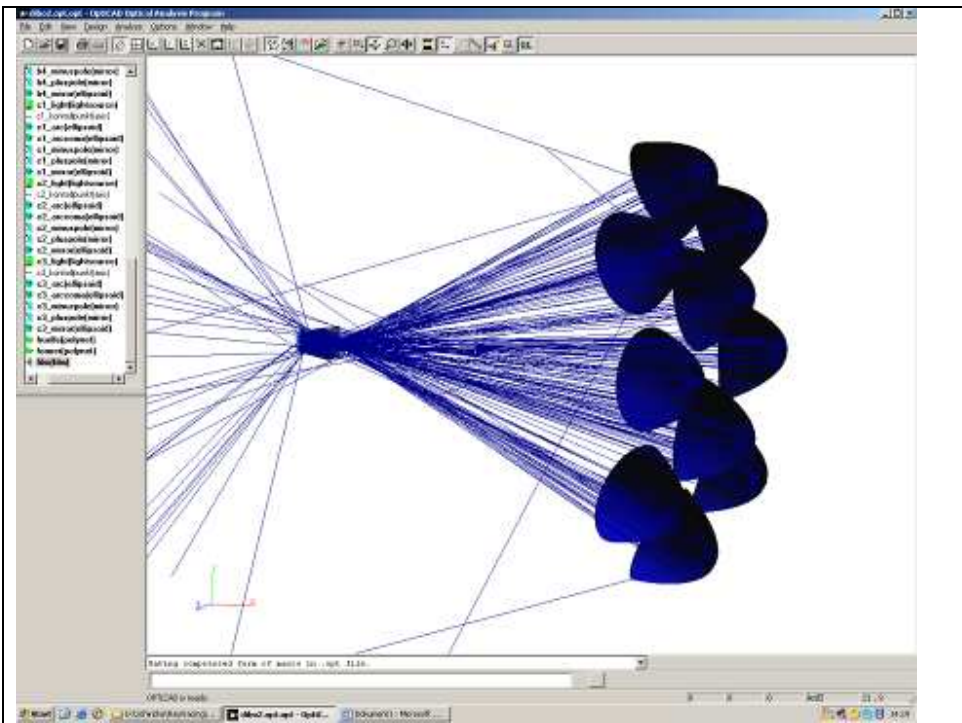
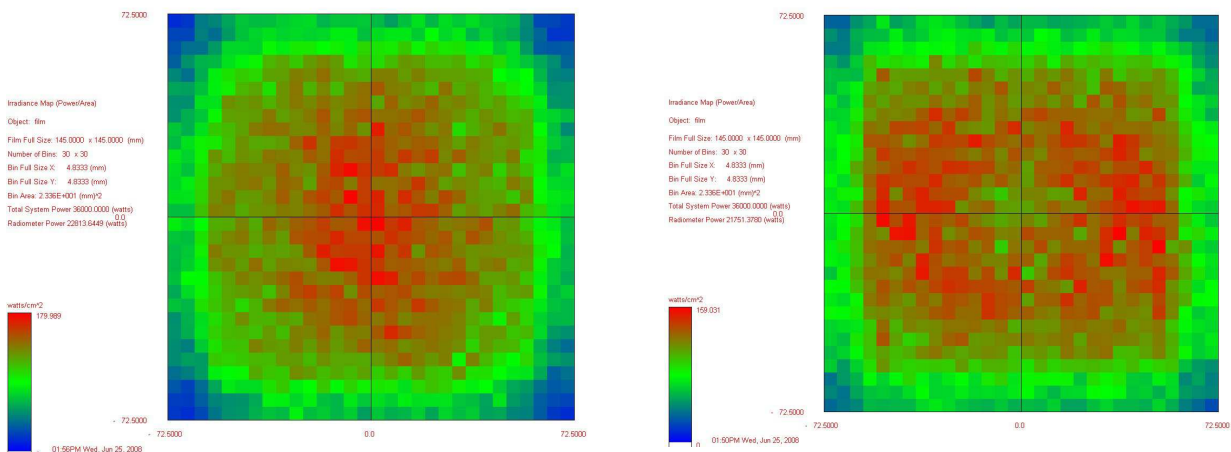


Figure 37

Example of OptiCAD<sup>®</sup> simulation of flux guide.

With the help of OptiCAD<sup>®</sup> the complete design of DLR's HFSS was emulated and different configurations of the flux guide were simulated. More than 50 parameter variations (edge length, distance to target, distance to focal spot and angles) were carried out to find an optimized configuration. In Figure 38 the flux distribution at the exit of the flux guide achieved for different configuration is reported.



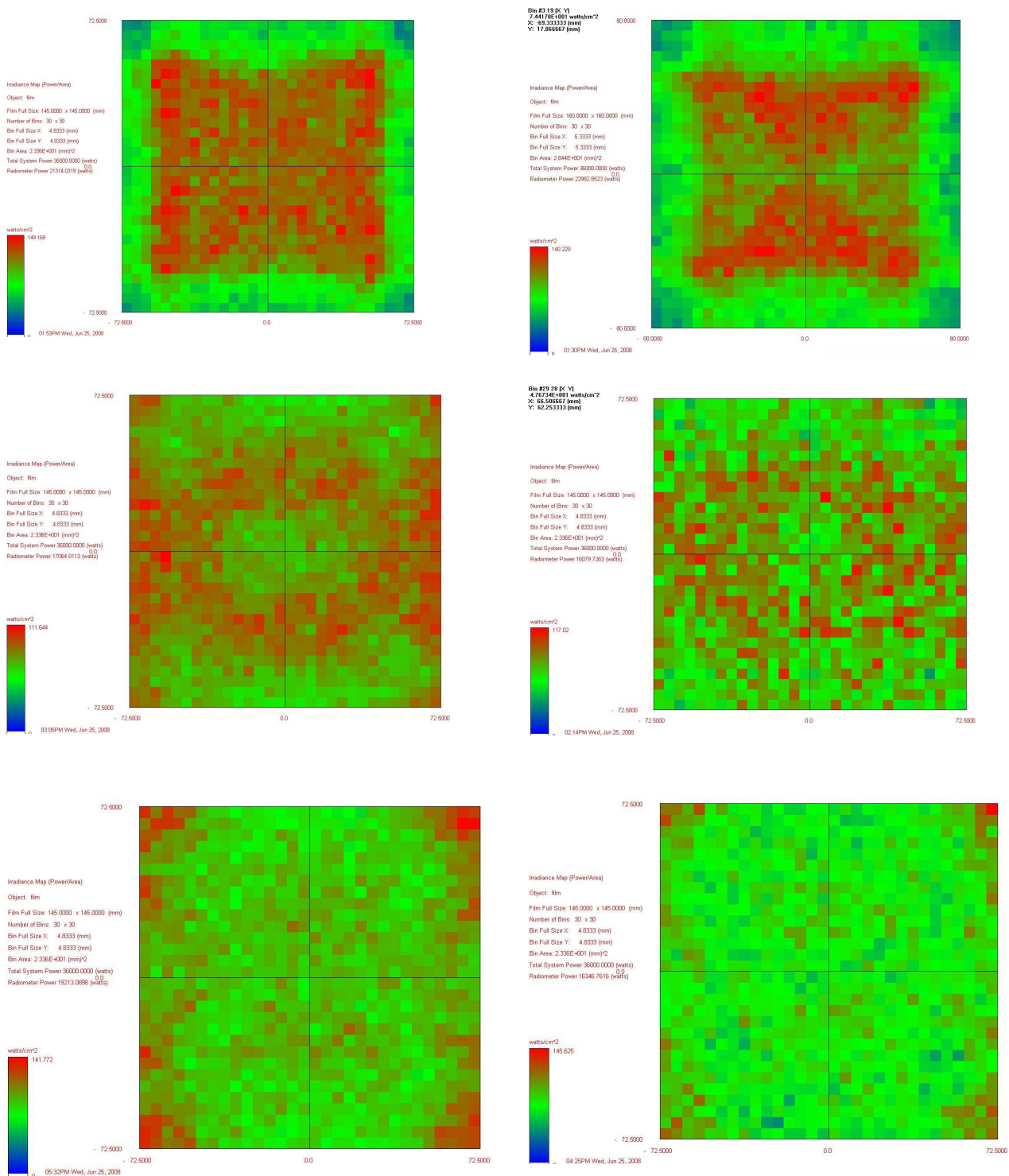


Figure 38:

Examples of the simulation for flux guide. Optimized flux distribution is reported on panel at lower/left.

The final (optimized) configuration of the flux guide that resulted from the parameter study is reported in Figure 39.

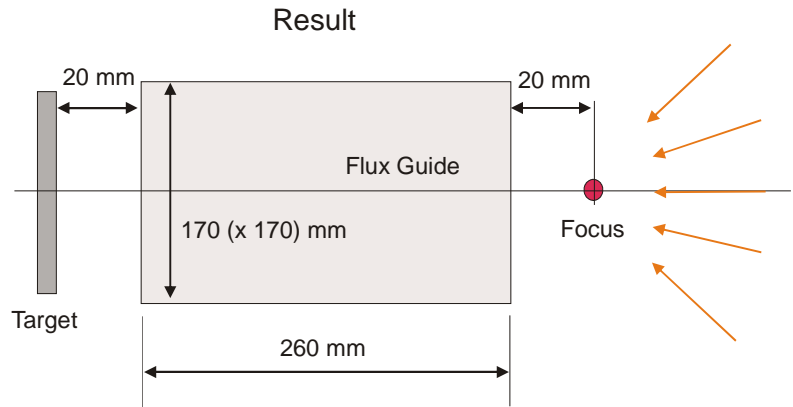


Figure 39:  
Optimized configuration of flux guide. Resulting flux distribution is reported in Figure 38 lower/left.

### 3.1.3 Defocusing

A new but actually obvious method to achieve a more uniform flux distribution on a larger target is to move the individual secondary foci slightly apart as depicted in Figure 40. Thus, the spots of the individual Xenon block are not anymore combined in a single spot but are now distributed over the target (see Figure 41).

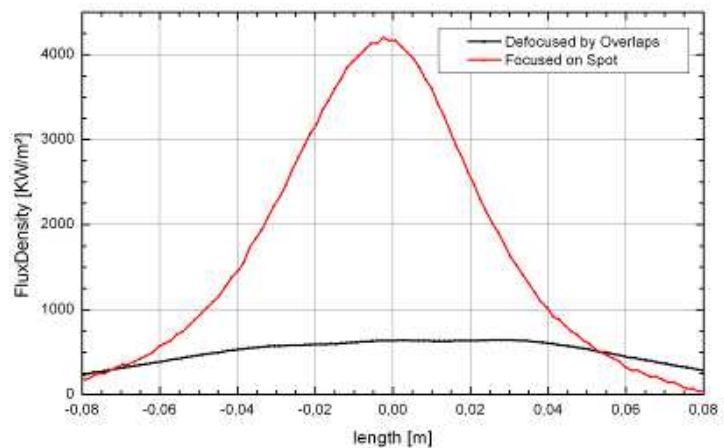
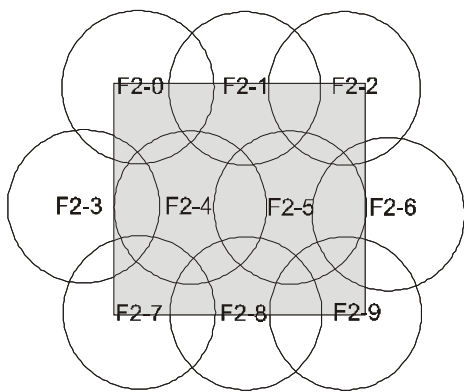
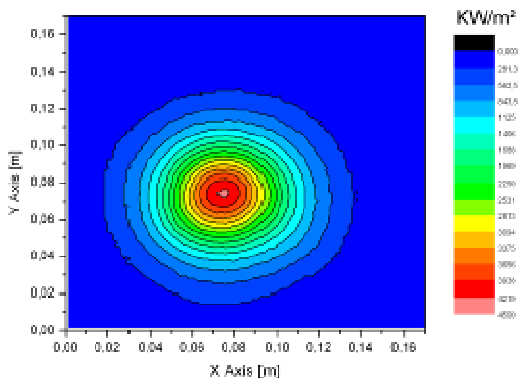


Figure 40:  
Secondary foci of lamps are distributed on target (gray).

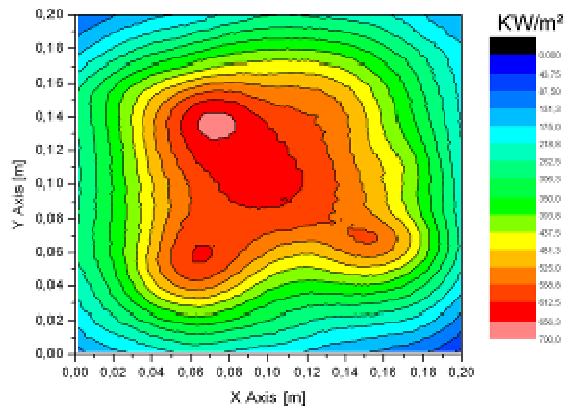
Figure 41:  
Comparison of flux distributions as a result of overlapping all foci (red) or distributing them according to Figure 40 (black) in

*DLR's HFSS.*

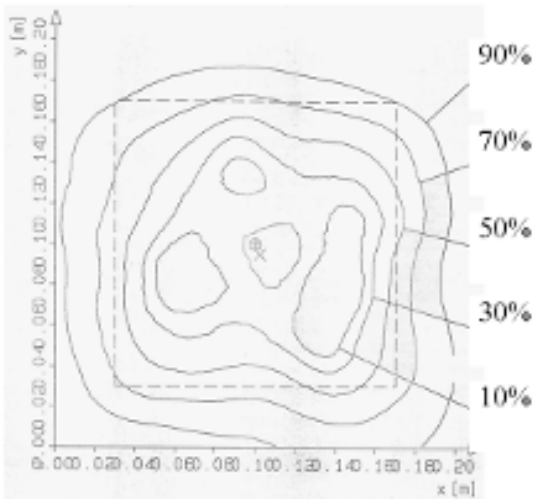
Defocusing as flux homogenization strategy was experimentally evaluated in a long term experiment at the DLR HFSS ("Ovabsol"). Defocusing was found to be a very effective method to flatten the Gaussian flux distribution and to be superior to a flux guide if the flux guide would obstruct the view onto the experiment. In the "Ovabsol" experiment it was required that the ceramic target (see Figure 45) of  $140 \times 140 \text{ mm}^2$  is homogeneously irradiated. Figures 42-44 and 46 illustrate the results.



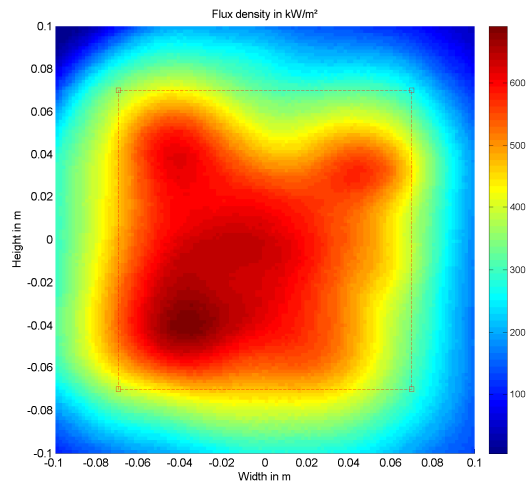
*Figure 42:*  
*Normal flux distribution.*



*Figure 43:*  
*Simulated flux distribution for "Ovabsol" experiment.*



*Figure 44:*  
*Measured flux density distribution on a  $140 \times 140 \text{ mm}^2$  target. 11 kW of a total of 17 kW fall within the dotted square symbolizing the aperture of the ceramic absorber.*



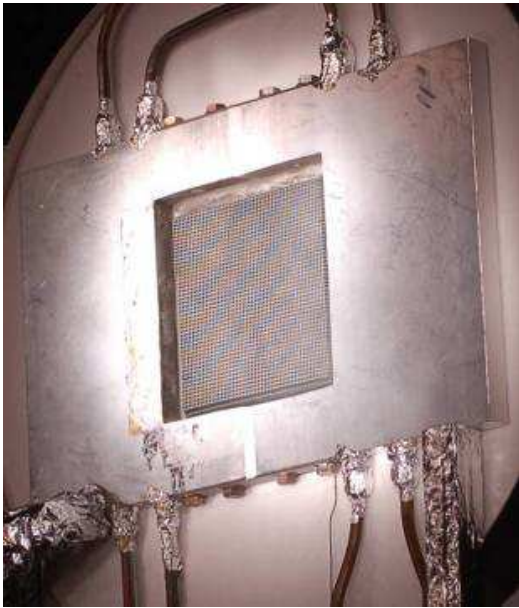


Figure 45:

*Ceramic absorber homogeneously irradiated at DLR's HFSS.*

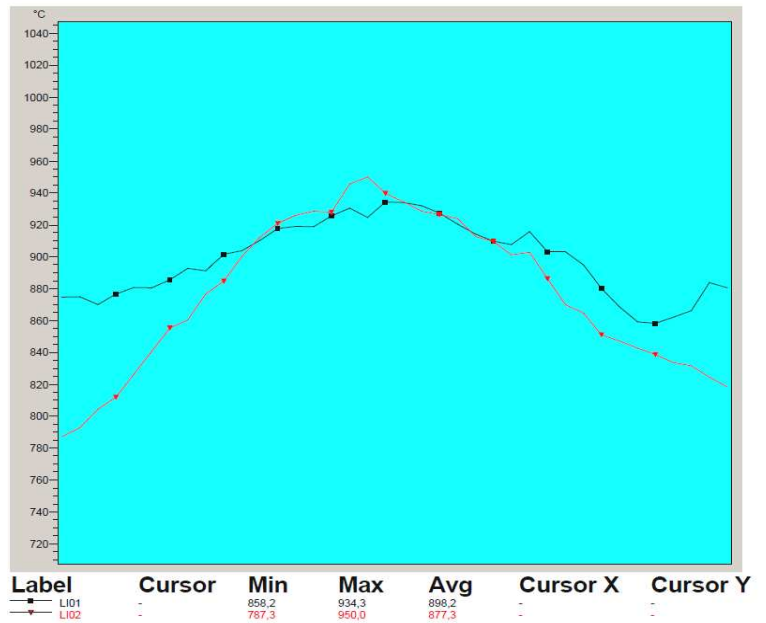


Figure 46:

*Cross sections through homogenized flux density distribution in the project "Ovabsol".*

### 3.2 Assessment of aging of simulator reflectors and arc lamps by performing periodic measurements

No specific long-term comparison is available yet for PSI's simulator as since it's commissioning first a protective window and later a venetian-blind type shutter was installed. Both have only a finite transmission and somewhat decrease the maximum power available at the spot. Furthermore, to increase the live time of the individual arc lamps (nominally rated at 600 h with each ignition having the effect of one operation hour according to the manufacturer), the maximum power level of each lamp was decreased from 15 kW<sub>el</sub> to 12.2 kW<sub>el</sub>. No noticeable decrease in performance that could be attributed to aging of either lamps or reflectors has been observed so far. Two lamps have since been replaced as they have surpassed their life time.

Due to space restriction at DLR ellipsoidal reflectors with a much higher eccentricity as compared to PSI's design had to be used to maintain the requirement of a 3 m focal length. This results in placing the lamp very close to the reflector (8 cm as compared to 20 cm in PSI's design). As a consequence much higher thermal loads are to be expected on the reflective coating of the ellipsoidal mirror (see Figure 47). The reflector is made from aluminum (Al99.5) with a thickness of 3 mm. To enhance its reflectivity beyond 90% the surface is coated by aluminum (evaporation) and additionally polished.

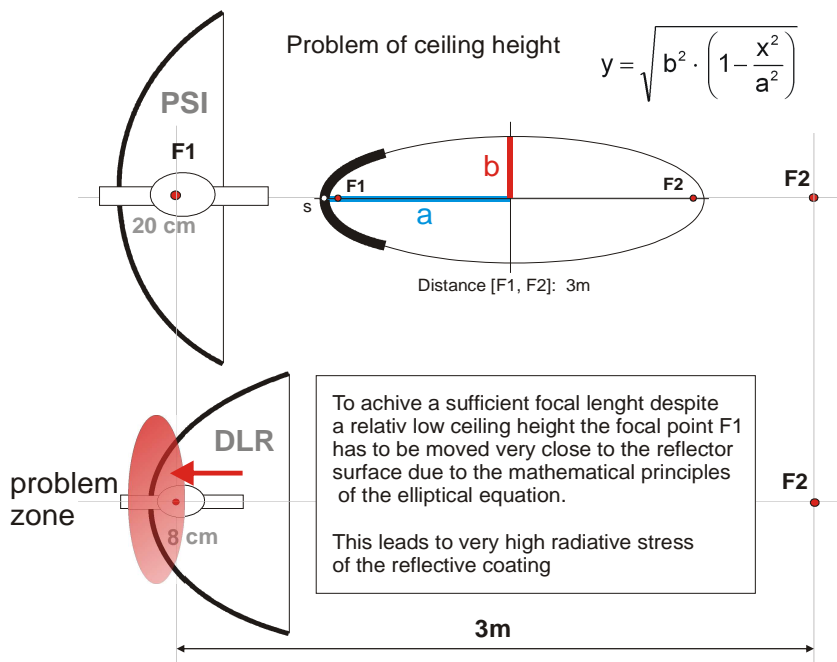


Figure 47:

Comparison of the geometries of the Xenon blocks at solar simulators installed at PSI and DLR.

After starting to operate the DLR's HFSS in 2007 it could be observed that the protective coating of the reflectors became damaged within in only a few weeks in the region of high thermal load (see Figure 48).



Figure 48:

Damage of reflective coating due to high thermal load.

Test samples with new coatings, new protective lacquers, and combinations thereof were obtained (see Figure 49) for testing their ability to withstand high thermal loads due to the high radiative flux impinging on them. The samples were tested by placing them close to the Xe arc lamps (see Figure 50)

used in the HFSS and irradiating them for several weeks. Stable combinations could be found. Damaged reflectors were freshly coated and incorporated at DLR's HFSS. No deterioration could be found since then while the solar simulated has been operated for several weeks. We are thus confident that the new coating is stable under our operating conditions.



*Figure 49:*

*Aluminum test strips different chemical compositions.*



*Figure 50:*

*Long term tests of the improved reflective coating.*

Both, for long term experiments and to estimate the maintenance costs the lamp performance as a function of time has to be known. During the long term experiment "Ovabsol" (Duration 10 month) at DLR's HFSS the aging of the Xenon arc-lamps was determined. Over a time period of 7 month the decrease of the lamp output power was noted as reported in Figure 51. We conclude from these results that the lifetime of Xenon arc-lamps used in a scientific environment is about half of the operation hours specified by the manufacturer (500 H instead of 1000 h).

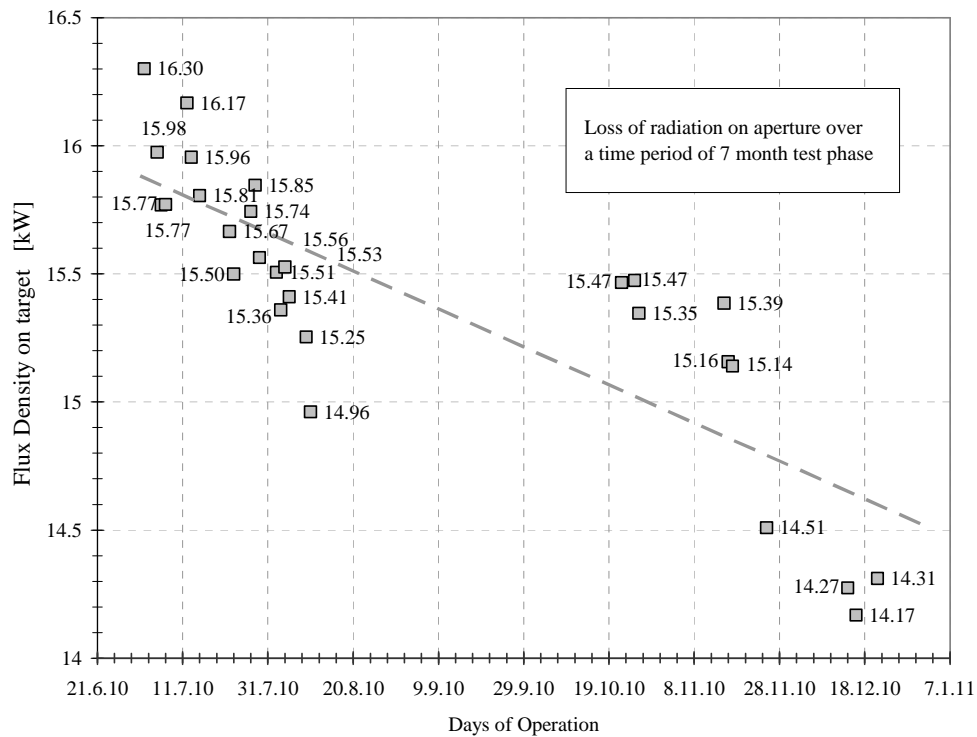


Figure 51:

Decrease of HFSS output measured by FATMES from July until December 2010. All measurements are recorded with all ten lamps in operation on a target of  $140 \times 140 \text{ mm}^2$  with a constant lamp current of 165 A. On October 22nd 2010 the lamps were new adjusted.

### 3.3 Pyrometric temperature measurement in solar simulators (PSI)

Pyrometric methods applicable in presence of external radiation must be able to either decompose the radiation detected into the external radiation reflected by the sample and the thermal emission of the sample or work in a wavelength interval where no external radiation is detected. FAMP (Flash-Assisted Multiwavelength Pyrometry) or pyro-reflectometry both belong to the first category while solar blind pyrometry belongs to the second. Due to its simplicity solar blind pyrometry is most widely used in solar furnaces. In solar simulators that use arc lamps as radiation source solar blind pyrometry is not feasible due to the continuous spectrum of the arc lamps (see Figure 52).

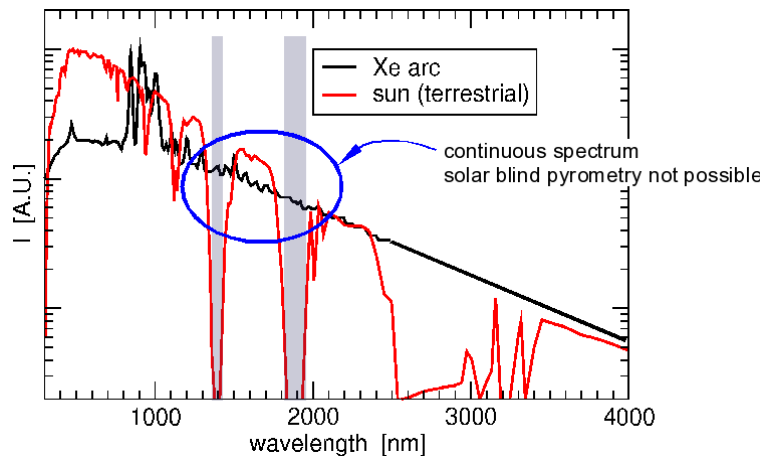
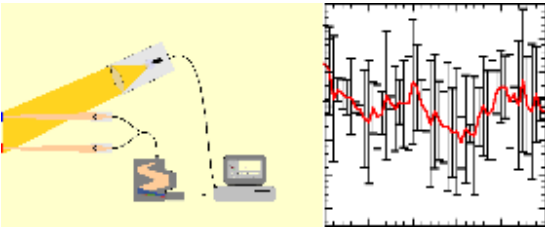
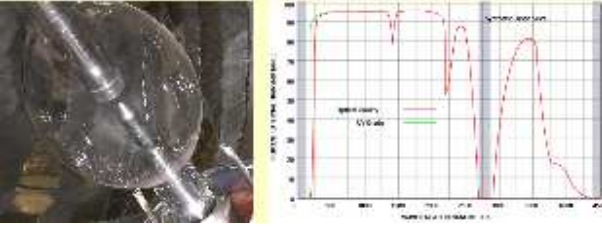
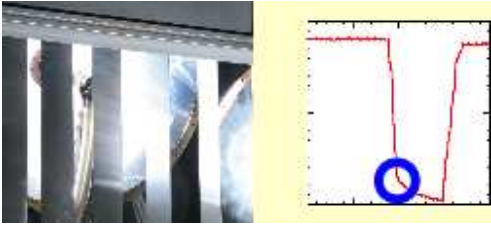
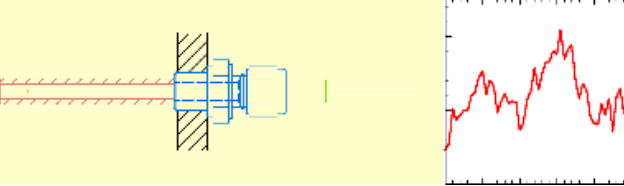


Figure 52: Comparison of a Xe arc lamp spectrum with a terrestrial solar spectrum.

In the following table methods available at present for temperature measurements in a solar simulator are listed:

	<p><b>FAMP / Pyro-reflectometry</b></p> <p>Complex method but delivers most detailed information. No beforehand knowledge of numerical values for the emissivity of the sample is required. (FAMP has been discontinued at PSI)</p>
	<p><b>Use bulb (/window) as filter</b></p> <p>Similar to solar blind pyrometry. Fused silica envelope (or protective window between arc lamps and sample) acts as filter blocking radiation in certain wavelength bands. If sample is placed behind (fused silica) window window temperature is measured.</p>
	<p><b>Pyrometry with intermittently closed shutter</b></p> <p>Simple but fast shutter is required. Thermal time constant of sample must be large compared to closure time of shutter.</p>
	<p><b>Shielded thermocouples</b></p> <p>Most simple method. Often requires some amount of modeling to convert measured temperature into temperature of sample.</p>

Most of the methods available are either complex or can be applied only in certain circumstances. A simple method that is universally applicable was not yet available. This prompted us to reassess the situation with the goal to come up with a new, simple pyrometric method that is generally applicable in solar simulators. This resulted in a new method its idea illustrated in Figure 53 (details see [3]): A conventional semiconductor detector detects the radiation coming from the sample. To improve the S/N ratio a phase sensitive detection scheme is applied that requires a chopper operating at a fixed frequency of  $\omega_2$ . The intensity of the arc lamp is independently modulated (direct electrical modulation of the output of its power supply) at a frequency  $\omega_1$  and is detected simultaneously using the identical optical train but a second lock-in amplifier that uses  $\omega_1$  as reference frequency. The detector measures the sum of the external radiation, electrically modulated at  $\omega_1$ , reflected at the sample with reflectivity  $R$ , and chopped at  $\omega_2$

$$I_{\text{ext}} = I_0^{\text{ext}} M_1 R M_2$$

and the thermal radiation emitted by the sample chopped at  $\omega_2$

$$I_{\text{th}} = I_0^{\text{th}} M_2$$

with  $M_i$  the two modulation functions. Separating the two signal components  $S_1$  and  $S_2$  at the two frequencies  $\omega_1$  and  $\omega_2$  yields

$$\begin{aligned} S_1 &\propto R I_0^{\text{ext}} \\ S_2 &\propto R I_0^{\text{ext}} + I_0^{\text{th}} \end{aligned}$$

After suitable calibration the thermal signal ( $I_0^{\text{th}}$ ) can be extracted as the difference of the two signals.

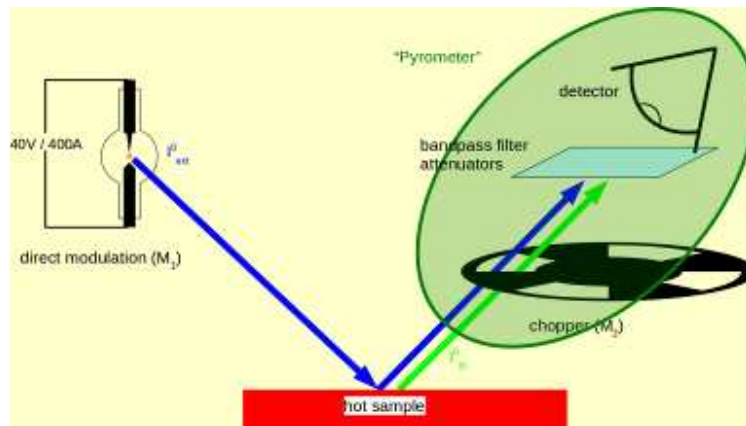


Figure 53: Pyrometry in presence of external radiation. Pyrometer (green ellipse) detects thermal emission (green) and reflected external radiation (blue) of arc lamp.

The method has been implemented in a laboratory setup with the sample placed in an electrically heated furnace. A 200 W arc lamp is used to simulate the external radiation. In Figure 54 the performance of the new method is illustrated for the lab setup. A surface-oxidized Sigradur G sample was used. The intensity external radiation, simulated by a focused 200 W arc lamp was changed as

indicated in the figure (a=0%, b=15%, c=34%, d=54%, e=100%). The blue curve represents the uncorrected temperature while the red curve represents the temperature obtained after subtraction of the external radiation.

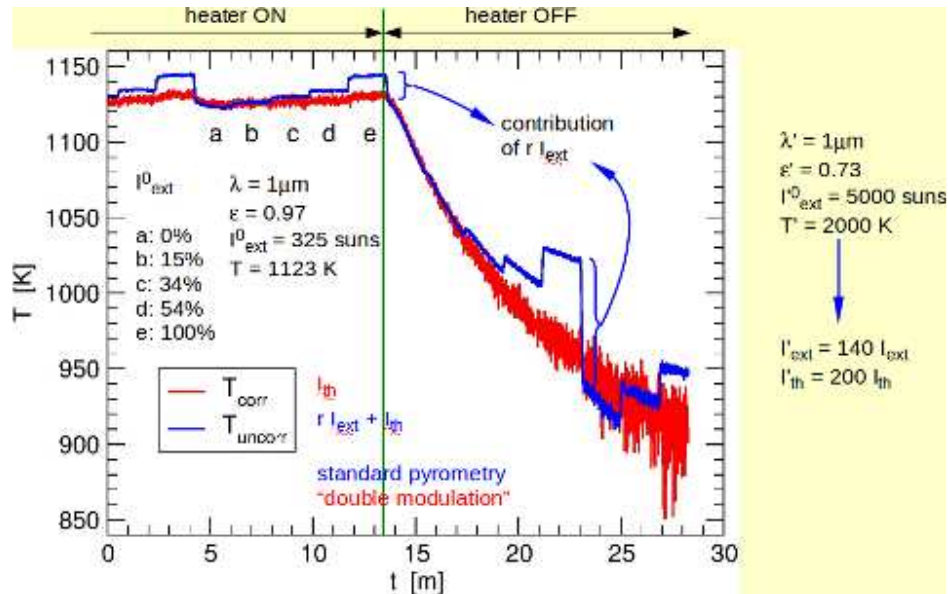


Figure 54: Separation of thermal radiation (red) from total radiation (blue) coming from sample.

While the output of the power supply for the 200 W arc lamp used in the laboratory setup could easily be modulated, modulation of the output of the rectifiers installed at PSI's solar simulator is more complicated. These 15 kW arc lamps are operated at around 30 VDC, 500 A. We are currently exploring ways to achieve this. Initial experiments using the remaining ripple at 300 and 600 Hz of the three-phase rectifiers were not successful as PSI's solar simulator is located in the close vicinity of a high voltage power line that emits too strong on these frequencies.

### 3.4 Avoidance of electromagnetic disturbances due to rectifiers and arc lamps

After initial worries, that this might pose a major problem, practical operation at DLR and PSI clearly shows that there are no major effects of such disturbances. Therefore this issue has not been elaborated further in the project.

## 4 Conclusions and recommendations for future high flux solar simulators

Based on construction, installation, testing and operation of the two solar simulators for several hundred hours some general conclusions and recommendations for future solar simulator projects can be formulated. Note, the weight that should be attributed to the individual recommendations for planning future simulators strongly depends on other boundary conditions such as e.g. budget or space available.

- Using ellipsoidal reflectors with a large eccentricity places the arc close to the reflector surface. A high thermal load on the reflector is to be expected and might lead to problems with the optical coating of the reflectors. Such problems, specifically peeling of the reflective coating in the vicinity of the lamp was initially observed at DLR's simulator but could be successfully solved by applying an optimized coating. At present, coatings seem to be available from a single manufacturer only and no generally applicable solution for the problem can be provided.
- Using air-cooled lamps that provide only about 50% of the output compared with water-cooled lamps simplifies the construction of the lamp / reflector units. Alignment of the individual lamps with respect to the ellipsoidal reflector becomes simpler and defocusing the lamp / reflector units to produce a more uniform flux distribution on a larger target becomes an option.
- The higher power provided by water-cooled lamps makes installation and alignment of the individual lamps in their reflectors more complicated. Producing a more uniform flux distribution on a larger target by defocusing becomes rather manpower intensive and was therefore never attempted at PSI.
- Both simulators use xenon short arc lamps with a similar spectrum. Still, both spectra exhibit a significant difference with regard to a solar spectrum. Generally, more radiation is present below about 500 nm and in the region of 800-1000 nm the strong xenon emission lines dominate the spectrum. This difference is less important for thermo-chemical experiments, most notably if performed in a cavity receiver, but may become relevant if the number of absorbed photons becomes important. This is the case in e.g. photovoltaics, photochemistry, or -catalysis.
- For long term experiments *that depend on the spectral distribution of power* it is important to determine the extent of the changes of the spectrum observed with aging of the lamps. This becomes even more important if a standardized measurement protocol is to be established and if results from different long term experiment have to be compared. At present, insufficient data is available for both simulators. DLR and PSI plan to repeat their respective measurements in a few years to address this point.
- Both simulators exhibit a significant output in the ultraviolet region of the spectrum (UVA and UVB) even after the radiation has passed through the protective window placed between the lamps and the spot. Thus, also the UVA and UVB levels of stray light produced by the sample / experiment will most likely surpass the exposure limits for artificial optical radiation as stated in [6, 7]. Therefore, whenever operation personnel has to be present close to the spot protective (UV blocking) eye wear should be worn and exposition to the skin should be minimized by wearing gloves or applying sunscreen. A detailed assessment of the UVA and UVB levels reached in the vicinity of the spot in any solar simulator is strongly suggested and is intended to be performed at the DLR and at PSI in the near future.
- Traditional solar-blind pyrometry can not be applied in a solar simulator due to its continuous spectrum. An alternative, specifically suited for application in a solar simulator has been demonstrated on a laboratory scale [3]. Applying this method in a solar simulator might be relatively straight forward if conventional three-phase rectifiers are used as is the case in PSI's simulator. These rectifiers usually exhibit a significant ripple at 300 and 600 Hz that is expected to modulate the output of the simulator at these frequencies. Unfortunately, PSI's solar simulator is located in the close vicinity of a high voltage power line that emits too strong on these frequencies preventing their use.

Overall the first years of operation of DLR's and PSI's first of their kind high flux solar simulators proved, that these instruments are very valuable tools in allowing weather independent testing under well defined and reproducible radiative conditions.

## References

- [1] H. Schmit; *Spatially resolved spectral characterisation of the focal region in the NIR at the HFSS*, Semester Thesis ETHZ (2011).
- [2] I. Alxneit and H. Schmit; *Spectral Characterization of PSI's High-Flux Solar Simulator*, submitted to J. Sol. Energy.-T. ASME (2011).
- [3] I. Alxneit; *Measuring temperatures in a high concentration solar simulator - Demonstration of the principle*, Sol. Energy. **85**, 516 (2011).
- [4] J. Petrasch, P. Coray, A. Meier, M. Brack, P. Haberling, D. Wullemin and A. Steinfeld; *A novel 50 kW 11,000 suns high-flux solar simulator based on an array of xenon arc lamps*, J. Sol. Energy.-T. ASME **129**, 405 (2007).
- [5] G. Dibowski, A. Neumann, P. Rietbrock, P. Willsch, J.-P. Säck, K.-H. Funken; *Der neue Hochleistungsstrahler des DLR - Grundlagen, Technik, Anwendung*, 10. Kölner Sonnenkolloquium (2007).
- [6] ICNIRP: *Guidelines on UV radiation exposure limits*. Health Physics **6**, 978 (1996).
- [7] ICNIRP: *Guidelines on limits of exposure to ultraviolet radiation of wavelengths between 180 nm and 400 nm (incoherent optical radiation)*. Health Physics **87**, 171 (2004).